

A likely planet-induced gap in the disk around T Cha

Nathanial P. Hendler,^{1*} Paola Pinilla,² Ilaria Pascucci,^{1,3} Adriana Pohl,^{4,5} Gijs Mulders,^{1,}
Thomas Henning,⁴ Ruobing Dong,² Cathie Clarke,⁶ James Owen,⁷ David Hollenbach⁸

¹Lunar and Planetary Laboratory, The University of Arizona, Tucson, AZ 85721, USA

²Department of Astronomy/Steward Observatory, The University of Arizona, 933 North Cherry Avenue, Tucson, AZ 85721, USA

³Earths in Other Solar Systems Team, NASA Nexus for Exoplanet System Science.

⁴Max Planck Institute for Astronomy, K  nigstuhl 17, D-69117 Heidelberg, Germany

⁵Heidelberg University, Institute of Theoretical Astrophysics, Albert-Ueberle-Str. 2, D-69120 Heidelberg, Germany

⁶Institute of Astronomy, University of Cambridge, Madingley Road, Cambridge, CB3 0HA, United Kingdom

⁷Institute for Advanced Study, Einstein Drive, Princeton, NJ 08540, USA

⁸SETI Institute, Mountain View, CA 94043, USA

29 November 2017

ABSTRACT

We present high resolution ($0.11'' \times 0.06''$) 3 mm ALMA observations of the highly inclined transition disk around the star T Cha. Our continuum image reveals multiple dust structures: an inner disk, a spatially resolved dust gap, and an outer ring. When fitting sky-brightness models to the real component of the 3 mm visibilities, we infer that the inner emission is compact (≤ 1 au in radius), the gap width is between 18–28 au, and the emission from the outer ring peaks at ~ 36 au. We compare our ALMA image with previously published $1.6\mu\text{m}$ VLT/SPHERE imagery. This comparison reveals that the location of the outer ring is wavelength dependent. More specifically, the peak emission of the 3 mm ring is at a larger radial distance than that of the $1.6\mu\text{m}$ ring, suggesting that millimeter-sized grains in the outer disk are located further away from the central star than micron-sized grains. We discuss different scenarios to explain our findings, including dead zones, star-driven photoevaporation, and planet-disk interactions. We find that the most likely origin of the dust gap is from an embedded planet, and estimate — for a single planet scenario — that T Cha’s gap is carved by a $1.2M_{\text{Jup}}$ planet.

Key words: protoplanetary disks — planet-disk interactions — circumstellar matter — planets and satellites: detection – planet and satellites: formation

1 INTRODUCTION

Transition disks are a sub-set of disks that display a significantly reduced near-infrared emission but large mid- to far-infrared emission in their spectral energy distribution (SED, Strom et al. 1989). This SED-identified characteristic is associated with a depletion of warm dust particles in the inner disk, which is why transition disks are thought to be crucial to understand how planet-forming material is cleared out.

Recently, many transition disks have been spatially resolved at different wavelengths revealing a variety of structures: gaps or cavities¹ (e.g. P  rez et al. 2014; Dong et al. 2017), spiral arms (e.g. Muto et al. 2012), shadows (some

of them variable with time, e.g. Pinilla et al. 2015a), and lopsided asymmetries (e.g. van der Marel et al. 2013; Casassus et al. 2013). These observations highlight that the SED-classified transition disks are a heterogeneous group of objects (e.g. Espaillat et al. 2014), only a subset of which may be truly caught in the act of dispersing (e.g. Ercolano & Pascucci 2017). For instance, disks shaped by planet-disk interaction are not necessarily dispersing as planet formation may occur early in disk evolution and be a long lived process.

The combination of near-infrared (tracing micron-sized particles) and millimeter imagery (mm/cm-sized grains) provides important insights into the origin of structures in transition disks. In particular, cavities and gaps resulting from pressure bumps in the gas are most pronounced at millimeter wavelengths as mm/cm-sized grains concentrate in pressure maxima, while micron-sized dust follows the gas (e.g. Brauer et al. 2008). In the case of planet-induced pressure bumps, the location of the peak emission at near-

* E-mail: equant@lpl.arizona.edu

¹ We use the term “gap” to refer to an empty or depleted annular region separating an inner and an outer disk while we use “cavity” for an empty or depleted region that extends from the central star out to an outer disk.

infrared and mm wavelengths can be also used to estimate the planet mass (e.g. [de Juan Ovelar et al. 2013](#); [Garufi et al. 2013](#)).

In this letter, we present ALMA 3 mm high-angular resolution ($0.11'' \times 0.06''$) observations of the transition disk around T-Chamaeleontis (T Cha). We also compare our data with the similarly high-resolution ($\sim 0.04''$) $1.6 \mu\text{m}$ SPHERE/VLT imagery recently published by [Pohl et al. \(2017\)](#). This comparison makes T Cha one of two systems, along with TW Hya ([van Boekel et al. 2017](#)), for which millimeter and near-infrared emission can be investigated at similar spatial scales (e.g. 2.5-4.3 au with SPHERE and 1.6-10 au with ALMA).

T Cha is a T-Tauri star (spectral type G8, [Alcala et al. 1993](#)) located in the ϵ -Cha association (at 107 ± 3 pc, [Gaia Collaboration et al. 2016](#)) with an estimated age between 2-10 Myr ([Fernández et al. 2008](#); [Ortega et al. 2009](#)). The presence of a gap in this disk was first inferred via SED modeling ([Brown et al. 2007](#)) and then later by the analysis of NIR interferometric data ([Olofsson et al. 2011, 2013](#)). High-resolution mid-infrared spectroscopy found evidence for a disk wind beyond the dust gap whose properties are compatible with a slow star-driven photoevaporative wind ([Pascucci & Sterzik 2009](#); [Sacco et al. 2012](#)). ALMA Cycle 0 observations at 0.85 mm could not resolve the gap but identified two emission bumps separated by 40 au, suggesting a cavity of 20 au in size ([Huélamo et al. 2015](#)). Interestingly, a candidate exoplanet has been reported inside the cavity ([Huélamo et al. 2011](#)), although its existence is debated ([Sallum et al. 2015](#)). The recent SPHERE/VLT scattered polarized light images ([Pohl et al. 2017](#)) resolve the outer ring-like emission. By fitting the observations with radiative transfer models, the inner edge of the outer ring is found at ~ 30 au. [Pohl et al. \(2017\)](#) also give upper limits for potential embedded planets. Using hot-start models, planets more massive than $\sim 8.5 M_{\text{Jup}}$ are ruled out at a distance from $0.1''$ to $0.3''$ (10.7 to 32.1 au) from the central star. At larger separations, the limit is $\sim 2.0 M_{\text{Jup}}$.

Here, we present our ALMA 3 mm observations (Sect. 2), then our visibility fitting approach (Sect. 3), and summarize our results, including the comparison with the SPHERE/VLT images (Sect. 4). We discuss our findings and address different origins for shaping the wavelength dependent size of gaps and cavities (Sect. 5). We conclude that the most likely explanation for T Cha's gap is from planet-disk interaction.

2 OBSERVATION AND DATA REDUCTION

Our ALMA Cycle 3 observations (Project ID: 2015.1.00979.S, PI I. Pascucci) were carried out on October 27 and 29, 2015 with 48 12 m antennas. Of the four Band 3 spectral windows, three were utilized for the continuum emission and one was centered around the hydrogen recombination line $\text{H}(41)\alpha$ at 92.03 GHz, which might trace a disk wind ([Pascucci et al. 2012](#)). The on-source time (~ 2 h) was set to achieve a sensitivity of $9 \mu\text{Jy}/\text{beam}$ in the aggregate continuum bandwidth of 6.6 GHz.

The ALMA data were calibrated using the Common Astronomy Software Applications (CASA, [McMullin et al. 2007](#)). The initial reduction scripts were provided by the

Symbol	Parameter	Range	Best Fit	Unit
Nuker Profile – Outer Disk				
R_{peak}	transition radius	[10–60]	37.09 ± 0.07	(au)
γ	inner disk index	[-6–1]	-3.10 ± 0.06	
α	transition index	[10–85]	53.73 ± 12.81	
β	outer disk index	[5–8]	6.49 ± 0.04	
Gaussian – Inner Disk				
A/B	amplitude ratio	[30–500]	336.0 ± 109.1	
R_{width}	gaussian width	[0–4]	1.01 ± 0.28	(au)

Table 1. Model parameters, parameter space (Range), and best fit modeling results.

North American ALMA Science Center and included phase, bandpass, and flux calibration. We ran the scripts using CASA 4.7.1 and created images in the continuum and in the line using Briggs weighting and robustness parameter equal to 0.5 (for the line we also applied a $2M\lambda$ tapering to increase the sensitivity). The continuum emission at an average frequency of 99.16 GHz (3.0 mm) is spatially resolved and detected at high sensitivity, see Figure 1 where the image rms is $9 \mu\text{Jy}/\text{beam}$ and the beam is $0.11'' \times 0.06''$ with a position angle of -18.11° . The H recombination line is not detected even when rebinning in spectral resolution to tens of km/s, the expected line width. Applying self-calibration did not significantly improve the continuum image while resulting in lower spatial resolution and did not lend a line detection. Hence, we will focus this letter on the properties of the continuum 3 mm emission using the non self-calibrated data.

On the image shown in Figure 1 we draw a 5σ contour and measure a total flux density of 16.5 ± 1.6 mJy (the quoted uncertainty includes an absolute flux calibration uncertainty of 10%). The peak S/N from our cleaned image is 110. Our value is ~ 2.5 higher than that found by ATCA at 3.2 mm ([Ubach et al. 2012](#)), which, in combination with the flux reported by [Huélamo et al. \(2015\)](#) (198 ± 4 mJy at 0.85 mm), results in a integrated millimeter spectral index of $\sim 1.97 \pm 0.08$. This value is close to the relationship between spectral index and cavity size introduced by [Pinilla et al. \(2014\)](#) for transition disks and could be an indication of mm-sized grains trapped at the outer edge of a planet-induced gap.

3 ANALYSIS

The T Cha 3 mm continuum map (hereafter: 3 mm image, Figure 1) reveals a disk with three distinct components: an inner emission, a spatially resolved gap, and an outer ring. In order to quantify the location and size of these structures we use two methods – fitting model radial profiles to the visibilities and direct measurements from the 3 mm image. We then compare our results with previously published findings at shorter wavelengths in order to examine the wavelength dependence of these features.

Assuming an axisymmetric disk, we model the sky brightness by fitting parametric models to the dust continuum emission in the visibility domain. To prepare the vis-

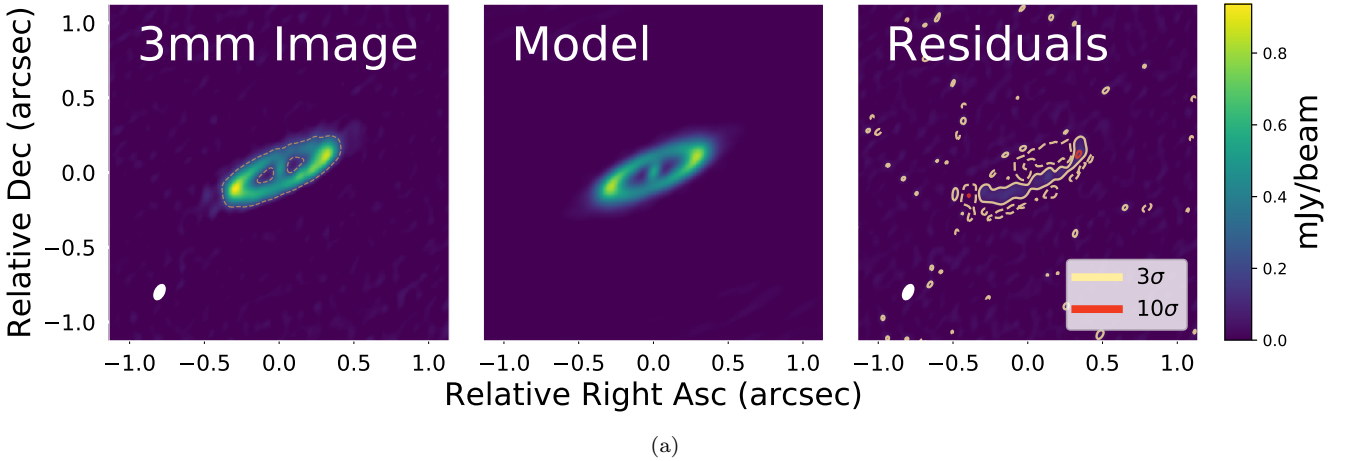


Figure 1. Left: Cleaned 3 mm ALMA image of *T Cha* (Project ID: 2015.1.00979.S). Beam is shown as ellipse in lower left and 1σ level is 1.6mJy. Contour shows 5σ region integrated for flux density measurement reported in Section 2. Center: Best-fit model. Right: The residuals of our best-fit model (center panel) subtracted from the unbinned ALMA image (left panel).

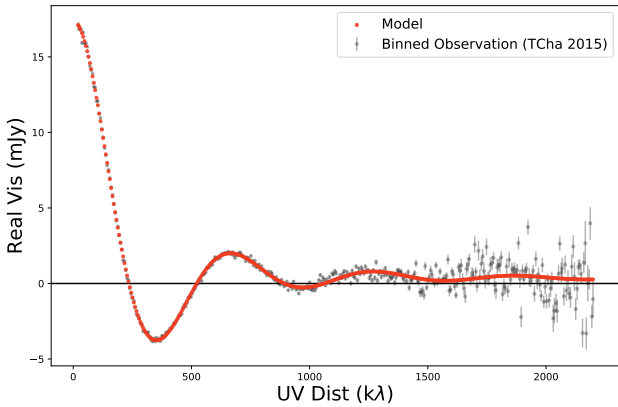


Figure 2. Deprojected real visibilities from Band 3 observation. Data are shown in gray with error bars. Model is overlaid in red.

ibilities for fitting, we center, deproject and bin the data. The visibilities were centered using the routines `uvmodelfit()` and `fixvis()` within CASA. CASA's disk model provided the best centering fit, resulting in a center with $\alpha_{ICRS} = 11^{\text{h}}57^{\text{m}}13.29^{\text{s}}$ and $\delta_{ICRS} = -79^{\circ}21^{\text{m}}31.68^{\text{s}}$. The observed (u, v) points from the three spectral windows are deprojected and binned, reducing the number of unflagged data points used for fitting from 7×10^7 to 3×10^4 . During this process, we minimize the residuals between the unbinned image and our axisymmetric binned image in order to find a fit for the inclination and position angle (PA). We find that the optimal values for the inclination and PA are 73° and 113° , respectively, which are within 2σ of the values and uncertainties reported in the literature (e.g. Olofsson et al. 2013; Pohl et al. 2017).

To model the three disk components, we assume radial intensity profiles that combine a Nuker profile and a Gaussian. Tripathi et al. (2017) showed that a Nuker profile (Lauer et al. 1995) reproduces well the visibilities of a variety of disks, including full and transition disks, with few input parameters. It does this by producing a decreasing monotone function for full disks, or a symmetric/asymmetric function

about a single maximum for rings. The addition of a Gaussian centered at the stellar location is necessary to fit the inner emission seen in Figure 1. The radial profile of our model is given by

$$I(r) = A \exp\left(-\frac{r^2}{2R_{\text{width}}^2}\right) + B \left(\frac{r}{R_{\text{peak}}}\right)^{-\gamma} \left[1 + \left(\frac{r}{R_{\text{peak}}}\right)^\alpha\right]^{(\gamma-\beta)/\alpha} \quad (1)$$

where the first term in the equation is the central Gaussian and the second term is the Nuker profile. In the equation, r is the radial distance and the remaining symbols are defined in Table 1. When Fourier transformed this symmetric brightness profile can be expressed with the zeroth-order Bessel function of the first kind J_0 (Berger & Segransan 2007). We then fit the model visibilities to the binned real part of the observed visibilities using the *emcee* (Foreman-Mackey et al. 2013) implementation of the Markov chain Monte Carlo method. For our radial grid, we use $r \in [0-500]$ au with steps of 0.025 au. Our parameter space is sampled with 1000 walkers having 500 steps each. The parameter space explored, and the results of our fitting are shown in Table 1. Posterior probability distributions of the sampled parameter space are available online.

Our best-fit model is imaged using the same (u, v) coordinates as our ALMA observations. Our model visibilities are shown in Figure 2, while Figure 1 shows the model image and the residuals between our unbinned observations and our best-fit model, i.e. data – model. Note that the residuals are at most 10σ , and below 1σ when we subtract the model from the binned data. Our residuals reveal a positive residual in the south spanning from east-to-west, and negative residuals in the south and north. Because positive and negative residuals are aligned with the disk major axis, we argue that this may result from optical-depth effects.

λ	Source	Location
3mm	Image R_{peak}	36.1±0.8 au
	Model R_{peak}	37.1 au
	Image R_{wall}	22.9 au
	Model R_{wall}	27.8 au
1.6 μm	Model R_{peak}	30.8 au
	Model R_{wall}	28.3 au

Table 2. Radial locations of the outer-ring emission found from images and best-fit models.

4 RESULTS

Radial intensity profiles along the disk’s PA of 113° are shown in Figure 3a for our ALMA 3mm image. We also compare in Figure 3b the best-fit model profiles from our visibility analysis and the best model fit to the SPHERE/VLT 1.6 μm image from Pohl et al. (2017). From these profiles we extract values for the location of the ring’s peak emission (R_{peak}). In addition to R_{peak} , we report R_{wall} defined as in de Juan Ovelar et al. (2013), i.e. the radial location where the intensity is half of the difference between the gap minimum intensity and the outer ring peak intensity. The radial position of R_{peak} resulting from our 3mm ALMA observations agree well (within 1 au) with our best-fit model (see Table 2). Comparing our visibility modeling with the NIR model provided by Pohl et al. (2017), we find that the 3mm R_{peak} is at a greater radial distance than the 1.6 μm R_{wall} by 8.8 au.

The central emission is unresolved by our beam of ~ 10 au diameter and our visibility modeling suggests that it is confined within a radius of only ~ 1 au. The flux density measured over the ALMA beam is 0.55 ± 0.06 mJy. By extrapolating the hot (1400K) NIR SED-component (Olofsson et al. 2013) out to 3mm, we find that only $\sim 2\%$ of the measured flux density could come from close-in micron-sized grains. In addition, from the long-wavelength portion of the SED (Pascucci et al. 2014) we calculate that no more than $\sim 30\%$ of the central emission arises from free-free emission. As such, most of the detected central emission is thermal dust emission, likely from millimeter-sized grains. By detecting the central 3mm emission *and* spatially resolving the outer ring, our ALMA image demonstrates that the disk of T Cha has a gap at millimeter wavelengths and not a cavity.

Using the definition of R_{wall} for the locations of the inner and outer edge of the gap, we estimate from our image a gap size of ~ 17.7 au. This should be considered a lower limit as we do not spatially resolve the central mm emission. The location of the gap’s outer edge found from our observation and modeling are 22.9 and 27.8 au respectively, with the latter being very similar to the 28.3 au reported by Pohl et al. (2017) from modeling the SPHERE images. By taking the model R_{wall} to be the location of the gap outer edge, we find an upper limit on the gap width of < 27.8 au (any larger and the gap would extend to zero au and become a cavity).

5 DISCUSSION

Our continuum ALMA observations reveal a disk around T Cha with three main dust components: an inner emission, gap, and an outer ring. By modeling the real part of the visibilities with a Nuker profile and a Gaussian, we can constrain the physical properties of these three components.

Our main result is the detection of an unresolved inner disk (≤ 1 au radius, based on visibility modeling), where most of the 3mm flux density arises from thermal dust emission, likely from mm-sized grains (see Sect. 4). This, combined with the already known outer emission, implies that the disk of T Cha has a gap in the population of millimeter-sized grains. Previous work has also inferred a very compact inner disk in the NIR ($R_{\text{out}} \leq 0.17$ au, Olofsson et al. 2011, 2013). Hence, whatever is the physical origin of the gap, it has to allow a detectable inner disk at multiple wavelengths.

The detection of a gap, and not of a cavity, in combination with other properties inferred from our analysis, enables us to exclude several mechanisms for the origin of the structures in the disk of T Cha. For instance, particle trapping at the outer edge of a dead zone can create structures as observed in transition disks (e.g. Flock et al. 2015; Ruge et al. 2016). Inside a dead zone, where turbulent velocities of particles are low, grain growth is efficient and small grains are depleted. As a result, we expect to observe a NIR and a mm-cavity of the same size. When an MHD disk wind acts together with a dead zone, smaller cavities will be present at shorter wavelengths. However, this latter scenario does not preserve a long-lived inner disk because the MHD wind removes efficiently the inner material, leaving a cavity, not a gap (Pinilla et al. 2016b). As a consequence, a dead zone, or a dead zone *and* MHD disk wind, is not a likely origin for the observed *gap* in the disk of T Cha.

A gap may originate from central star-driven photoevaporation (second disk evolutionary stage in Figure 6 of Alexander et al. 2014). While there is evidence in T Cha of a disk wind that can be photoevaporative in nature (Pascucci & Sterzik 2009; Sacco et al. 2012), photoevaporation predicts only a specific combination of mass accretion rate and gap size (see Figure 6 in Ercolano & Pascucci 2017). T Cha shows strong photometric variability and UX Ori-like behavior, inferred from significant changes of prominent emission lines, such as H_α . If this variability is due to accretion episodes, the mean accretion rate of T Cha is $4 \times 10^{-9} M_\odot/\text{year}$ (Schisano et al. 2009). With this mass accretion rate and our gap size estimate ≥ 20 au, star-driven photoevaporation does not appear to be a plausible mechanism to open the gap seen in the T Cha disk. This argument is valid even in the presence of variability because the timescale for the hole to grow from the initial gap opening radius to ~ 20 au is longer than the timescale for draining material by accretion. If the accretion rate in the outer disk is variable then there will be episodes when the inner disk refills and there is accretion onto the star, which will reduce the gap size.

Both cavities and gaps are expected from planet-disk interactions. While a cavity can be opened by a massive planet, Pinilla et al. (2016a) demonstrated that an inner disk can be maintained at timescales greater than 1 Myr for planets of mass $\sim 1.0 M_{\text{Jup}}$. More massive planets filter out all kind of grains (from micron- to mm/cm-sized particles),

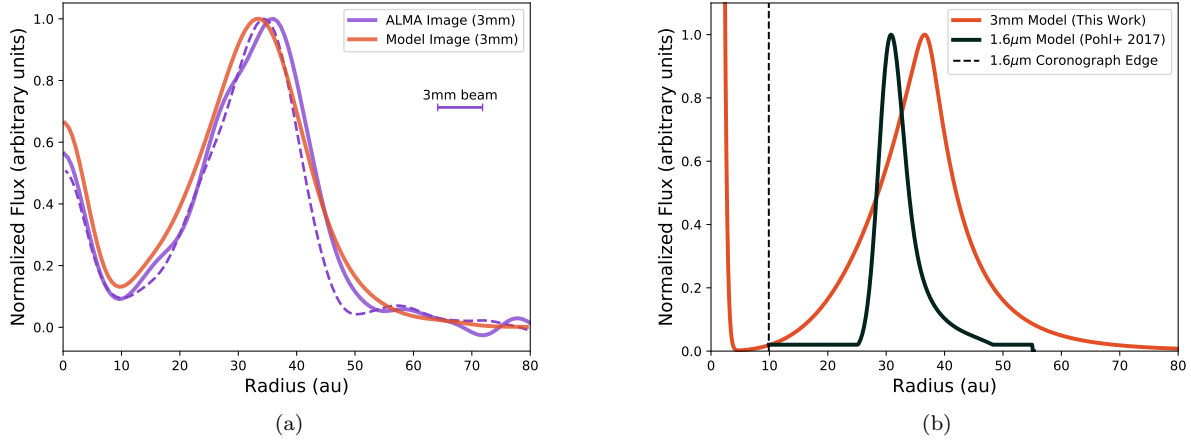


Figure 3. (a) Comparison of radial intensities profiles (normalized to the intensity of the ring peak) from our ALMA image and best-fit model image (using same u, v spacing). For the ALMA image (purple), the solid line is taken radially along T Cha's PA towards the NE, while the dashed lines is taken along the same line extending to the SW. Because our model is axisymmetric, we show only one profile (red). The ALMA/3mm beam width along T Cha's PA is $0.072''$. (b) Comparison of ring location at different wavelengths. Radial intensities taken from best-fit models.

and as a result the inner disk is gone after few million years of evolution.

The spatial segregation of small and large particles seen in T Cha, as observed in the NIR and mm-emission respectively, is another expected outcome of planet-disk interactions, because the small grains are expected to follow the gas while the large grains move and accumulate in pressure maxima. Indeed, radial segregation of small vs. large grains has been observed in different transition disks following the expected results from planet-disk interaction models (Garuffi et al. 2013; Pinilla et al. 2015b). Using the wavelength-dependent grain size relationships resulting from the 2D hydrodynamical and dust evolution models of de Juan Ovelar et al. (2013), we can constrain the mass of the potential embedded planet inside the gap. With the values reported in Table 2, we find $R_{\text{wall,NIR}}/R_{\text{peak,mm}} = 0.8$ which implies a $1.2 M_{\text{Jup}}$ planet in the single-planet scenario and with the specific disk properties assumed in de Juan Ovelar et al. (2013) (model outcomes are sensitive to disk properties, especially viscosity). The planet mass is consistent with the upper limits reported in Pohl et al. (2017), leaving open the possibility that the gap in the disk of T Cha is carved by a giant planet.

While a large millimeter gap can be consistent with a single planet, Dong & Fung (2017) show that the width of a single-planet gap observed at near-infrared wavelengths should be only $\sim 30 - 40\%$ of the gap radial location. Using $R_{\text{wall,NIR}}$ from Table 2 and the coronagraph mask diameter of 185 mas gives a minimum NIR gap width of ~ 18 au, which is $\geq 64\%$ of the gap's radial location. As such it is unlikely that the gap in the disk of T Cha is opened only by one planet. Rather multiple embedded planets, whose individual gaps overlap, contribute to open the large observed gap.

In summary, we find that the most likely origin for the gap in the disk of T Cha is due to planet-disk interactions. If the gap is carved by a single planet, we find that a mass of $1.2 M_{\text{Jup}}$ is required. However, because of the large gap

width, multiple less massive planets with overlapping gaps are more probable. Future ALMA observations could constrain the size of a potential gap in the gas surface density (e.g. van der Marel et al. 2016), which is crucial to distinguish between single or multiple planets (e.g. Zhu et al. 2011).

ACKNOWLEDGEMENTS

We thank the anonymous referee for useful comments and suggestions. I.P. and N.H. acknowledge support from an NSF Astronomy & Astrophysics Research Grant (ID: 1515392). P.P. acknowledges support by NASA through Hubble Fellowship grant HST-HF2-51380.001-A awarded by the Space Telescope Science Institute, which is operated by the Association of Universities for Research in Astronomy, Inc., for NASA, under contract NAS 5-26555. This paper makes use of the following ALMA data: ADS/JAO.ALMA#2015.1.00979.S. ALMA is a partnership of ESO (representing its member states), NSF (USA) and NINS (Japan), together with NRC (Canada), MOST and ASIAA (Taiwan), and KASI (Republic of Korea), in cooperation with the Republic of Chile. The Joint ALMA Observatory is operated by ESO, AUI/NRAO and NAOJ. The NRAO is a facility of the NSF operated under cooperative agreement by Associated Universities, Inc.

REFERENCES

- Alcala J. M., Covino E., Franchini M., Krautter J., Terranegra L., Wichmann R., 1993, *A&A*, **272**, 225
- Alexander R., Pascucci I., Andrews S., Armitage P., Cieza L., 2014, *Protostars and Planets VI*, pp 475–496
- Berger J. P., Segransan D., 2007, *New Astron. Rev.*, **51**, 576
- Brauer F., Dullemond C. P., Henning T., 2008, *A&A*, **480**, 859
- Brown J. M., et al., 2007, *ApJ*, **664**, L107
- Casassus S., et al., 2013, *Nature*, **493**, 191

- Dong R., Fung J., 2017, *ApJ*, **835**, 146
- Dong R., et al., 2017, *ApJ*, **836**, 201
- Ercolano B., Pascucci I., 2017, *Royal Society Open Science*, **4**, 170114
- Espaillet C., et al., 2014, *Protostars and Planets VI*, pp 497–520
- Fernández D., Figueras F., Torra J., 2008, *A&A*, **480**, 735
- Flock M., Ruge J. P., Dzyurkevich N., Henning T., Klahr H., Wolf S., 2015, *A&A*, **574**, A68
- Foreman-Mackey D., Hogg D. W., Lang D., Goodman J., 2013, *PASP*, **125**, 306
- Gaia Collaboration et al., 2016, *A&A*, **595**, A2
- Garufi A., et al., 2013, *A&A*, **560**, A105
- Huélamo N., Lacour S., Tuthill P., Ireland M., Kraus A., Chauvin G., 2011, *A&A*, **528**, L7
- Huélamo N., de Gregorio-Monsalvo I., Macias E., Pinte C., Ireland M., Tuthill P., Lacour S., 2015, *A&A*, **575**, L5
- Lauer T. R., et al., 1995, *AJ*, **110**, 2622
- McMullin J. P., Waters B., Schiebel D., Young W., Golap K., 2007, in Shaw R. A., Hill F., Bell D. J., eds, *Astronomical Society of the Pacific Conference Series Vol. 376, Astronomical Data Analysis Software and Systems XVI*. p. 127
- Muto T., et al., 2012, *ApJ*, **748**, L22
- Olofsson J., et al., 2011, *A&A*, **528**, L6
- Olofsson J., et al., 2013, *A&A*, **552**, A4
- Ortega V. G., Jilinski E., de la Reza R., Bazzanella B., 2009, *AJ*, **137**, 3922
- Pascucci I., Sterzik M., 2009, *ApJ*, **702**, 724
- Pascucci I., Gorti U., Hollenbach D., 2012, *ApJ*, **751**, L42
- Pascucci I., Ricci L., Gorti U., Hollenbach D., Hendler N. P., Brooks K. J., Contreras Y., 2014, *ApJ*, **795**, 1
- Pérez L. M., Isella A., Carpenter J. M., Chandler C. J., 2014, *ApJ*, **783**, L13
- Pinilla P., et al., 2014, *A&A*, **564**, A51
- Pinilla P., et al., 2015a, *A&A*, **584**, L4
- Pinilla P., et al., 2015b, *A&A*, **584**, A16
- Pinilla P., Klarmann L., Birnstiel T., Benisty M., Dominik C., Dullemond C. P., 2016a, *A&A*, **585**, A35
- Pinilla P., Flock M., Ovelar M. d. J., Birnstiel T., 2016b, *A&A*, **596**, A81
- Pohl A., et al., 2017, *A&A*, **605**, A34
- Ruge J. P., Flock M., Wolf S., Dzyurkevich N., Fromang S., Henning T., Klahr H., Meheut H., 2016, *A&A*, **590**, A17
- Sacco G. G., et al., 2012, *ApJ*, **747**, 142
- Sallum S., et al., 2015, *ApJ*, **801**, 85
- Schisano E., Covino E., Alcalá J. M., Esposito M., Gandolfi D., Guenther E. W., 2009, *A&A*, **501**, 1013
- Strom K. M., Strom S. E., Edwards S., Cabrit S., Skrutskie M. F., 1989, *AJ*, **97**, 1451
- Tripathi A., Andrews S. M., Birnstiel T., Wilner D. J., 2017, *ApJ*, **845**, 44
- Ubach C., Maddison S. T., Wright C. M., Wilner D. J., Lommen D. J. P., Koribalski B., 2012, *MNRAS*, **425**, 3137
- Zhu Z., Nelson R. P., Hartmann L., Espaillat C., Calvet N., 2011, *ApJ*, **729**, 47
- de Juan Ovelar M., Min M., Dominik C., Thalmann C., Pinilla P., Benisty M., Birnstiel T., 2013, *A&A*, **560**, A111
- van Boekel R., et al., 2017, *ApJ*, **837**, 132
- van der Marel N., et al., 2013, *Science*, **340**, 1199
- van der Marel N., van Dishoeck E. F., Bruderer S., Andrews S. M., Pontoppidan K. M., Herczeg G. J., van Kempen T., Miotello A., 2016, *A&A*, **585**, A58

This paper has been typeset from a $\text{T}_{\text{E}}\text{X}/\text{L}^{\text{A}}\text{T}_{\text{E}}\text{X}$ file prepared by the author.